Self-organized nanostructuring in $Zr_{0.69}Al_{0.31}N$ thin films studied by atom probe tomography

L.J.S. Johnson[a], N. Ghafoor[a], D. Engberg[a], M. Thuvander[b], K. Stiller[b], M. Odén[a], and L. Hultman[a]

[a]Department of Physics, Chemistry and Biology (IFM), Linköping University, SE-581 83 Linköping, Sweden

[b]Department of Applied Physics, Chalmers University of Technology, SE-421 96 Göteborg, Sweden

Abstract

We have applied atom probe tomography to analyze the self-organizing structure of wear-resistant $Zr_{0.69}Al_{0.31}N$ thin films grown by magnetron sputtering. Transmission electron microscopy shows that these films grow as a three-dimensional nanocomposite, consisting of interleaved lamellae in a labyrinthine structure, with an in-plane size scale of ~ 5 nm. The structure was recovered in the Al APT signal, while the Zr and N data lacked structural information. The onset of the self-organized labyrinthine growth was observed to occur locally by nucleation, at 5-8 nm from the MgO substrate, after increasing Zr-Al compositional fluctuations. At a later stage, the labyrinthine growth mode was observed to occasionally break down and form larger ZrN grains.

Introduction

Atom probe tomography (APT) is a powerful technique for resolving chemical structure on an atomic scale. Its application has, however, essentially been limited to bulk metals. In recent years technical advances, including laser pulsing, the local electrode, and FIB sample preparation, which collectively are referred to as the second revolution of APT [1], have extended the applicability to most inorganic materials. Focus is therefore given to ceramics, and among the issues now being tackled is nano-scale structure formation and evolution in such materials.

Nanostructuring in transition metal nitrides can be, and has been, used for surface engineering, e.g. to improve the wear-resistance of thin films. Important examples are the spinodal decomposition in the Ti-Al-N system [2-4] and the TiN-SiN phase separation in Ti-Si-N [5-7]. The basis of self-organization in these and related systems is the large thermodynamical driving forces for separation caused by substantial miscibility gaps when mixing non-isostructural nitrides. A better understanding of the separation process would guide in thrive to fully utilize the potential of this effect.

Following large-scale application of TiAlN coatings, attention has been turning towards transition metal (TM)-nitrides formed with Zr [8] or Hf [9] instead of Ti, as those elements are similar in electronic structure but, with increasing size and mass, providing systems with even larger miscibility gaps. Estimations based on 0 K calculations yield an enthalpy of mixing for cubic Zr-Al-N about twice that of Ti-Al-N [10]. This is borne out in experiments as it has not been possible to synthesize cubic

B1 solid-solution $Zr_{1-x}Al_xN$ with x larger than approximately 0.3 [11], whereas $Ti_{1-x}Al_xN$ films with x up to ~0.7 are readily synthesized [12].

While studying the Zr-Al-N system using magnetron sputter epitaxy, it was discovered that deposition of $Zr_{0.64}Al_{0.36}N$ under conditions optimized for epitaxy of ZrN on MgO(001) substrates results in a two-phase labyrinthine nanostructure [13]. Transmission electron microscopy (TEM) resolved the structure as standing lamellae of fcc-ZrN and h-AlN. Some questions remain to be answered, e.g. the initial stages of self-organization during growth and the phase purity of the lamellae.

Here, APT was used to study the nanostructure formation in $Zr_{0.64}Al_{0.36}N$ thin films, including its full three-dimensional form as well as the initial growth at the substrate. Comparison with previous TEM-work [13] also allows for an evaluation of the APT reconstruction, as the structure differs significantly from the basic assumptions underlying the current APT-reconstruction protocols. A study of the very first few nanometers of growth from the substrate is conducted, in which a transformation is observed from disordered separation to organized growth. Finally, limits of the labyrinthine growth due to perturbation by renucleation events are discussed.

Experimental Details

$Zr_{0.69}Al_{0.31}N$ thin films were deposited by reactive magnetron sputtering from elemental targets in an Ar/N_2 atmosphere at 0.6 Pa The background pressure was < $4x10^{-5}$ Pa. The substrate was MgO(001) kept at 800 or 900 °C during depositions. Further details on the deposition parameters are given in Ref. [13].

Samples for transmission electron microscopy were prepared by mechanical grinding and polishing, followed by ion polishing using a Gatan PIPS. TEM was performed

using a FEI Tecnai G2 TF20 U-Twin microscope, operated at 200 kV. Scanning TEM (STEM) images were recorded with a high angle annular dark field (HAADF) detector.

The average composition and the level of impurities in the films were determined by time-of-flight elastic recoil detection analysis (TOF-ERDA) carried out at the Uppsala University tandem accelerator, using a 40 MeV $^{127}I^{9+}$ beam at 67.5° incidence relative to the surface normal and a 45° recoil angle.

Atom probe tomography sample tips were prepared by focused ion beam milling with a Zeiss Crossbeam ES-1540 using Ga ions, after the protocol of Thompson et al. [14]. Tips were mounted on prefabricated Si posts on a wafer, followed by annular milling at 30 kV with a finishing step at 5 kV. The samples were analyzed using an Imago (now Cameca) LEAP 3000X HR atom probe running in laser mode, using a green laser at a wavelength of 532 nm. The base temperature was kept at 60 K, the laser energy at 0.3 nJ/pulse, and the pulse rate at 200 kHz. The evaporation rate was regulated at 0.05 ions/pulse. The APT datasets were reconstructed using Cameca IVAS 3.4 in voltage reconstruction mode.

Results and Discussion

Atom probe behavior and overall composition

A typical mass spectrum from the ZrAlN films is shown in Fig. 1. The dominating peaks are ZrN^{2-3+}, Zr^{2-4+} Al^{1-3+}, N^+, and N_2^+. There is also a peak at 40 Da, which corresponds to Ar^+ from the sputter deposition. The tails are moderate and most peaks are well resolved, e.g., the Al^{2+}-N^+ pair at 13.5 and 14 Da overlap at less than 1 % of the Al^{2+} peak height. This may be compared with published spectra of Ti-Si-N [15] or

Ti-Al-N [3, 16], where the peaks are significantly broader. As the electronic structure is similar, as well as the APT analysis conditions, it is most likely differences in thermal conductivity that are the cause of the difference in peak broadening. The examples cited had a defect-rich microstructure and were nanocrystalline or finely columnar. The present films were grown under epitaxial growth conditions. Their higher crystal quality leads to a corresponding increase in thermal conductivity, and furthermore, the probable presence of relatively pure ZrN, which by analogy with Ti-Al-N would be more conductive than when alloyed with Al [17], will also contribute to a better thermal transport.
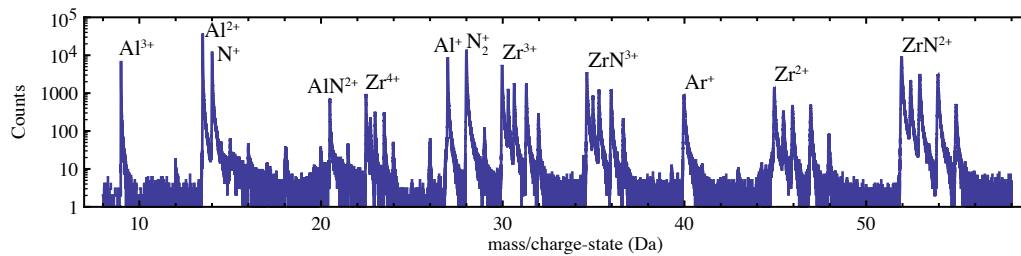
Figure 1: Atom probe mass spectrum of sputtered $Zr_{0.64}Al_{0.36}N$.

Kingham analyses, where the observed ratio of charge states for an element is compared to theoretical predictions of quantum tunneling which depend on the applied electric field, of the Zr and Al charge state ratios [18], with the assumption of a single evaporation field, do not give consistent results, neither for Zr and Al separately nor collectively. The present films are known to consist predominantly of two phases in the nanolabyrinthine parts [13], and according to Kingham's diagrams it is unlikely that there are three separate charge states present for the same evaporation field, a two-field model was applied by considering the mass spectrum as the sum of two contributions: Al^+ & Al^{2+}, and Al^{2+} & Al^{3+} for Al, and Zr^{2+} & Zr^{3+}, and Zr^{3+} & Zr^{4+} for Zr. This yielded the fields 25 and 40 V/nm for Al, and 30 and 46 V/nm for Zr. The particular assignment of parts of the main peak to either phase

changed the fields by no more than ±1 V/nm except for the pathological corner cases of assigning the whole peak to one of the phases. An evaporation field of ~40 V/nm is quite consistent with those reported for TiAlN [3] at similar conditions. No values for AlN were found in the literature, but the bonds in wurtzite-AlN are known to be weaker than that of TiN (and, likely, by electronic structure similarity with ZrN) from theoretical calculations [19] and phase decomposition temperatures. The fraction of multiple evaporation events was ~50 % during the runs, which again is congruent with reported values for TiN-based films [3, 15, 16, 20].

Table 1: Composition of $Zr_{1-x}Al_xN$ thin films measured by APT and TOF-ERDA: for the APT measurements the average of four runs along with an interval of ± 2 estimated standard deviations are given.

Technique	$x = $ Al/(Al+Zr) (%)	N (at. %)	Ar (at. %)	O (at. %)
APT	31.0 ± 1.3	46.8 ± 1.1	0.99 ± 0.17	0.19 ± 0.29
TOF-ERDA	30.8	47.6	0.2	1.7

The mean composition measured by APT is given in Table 1 along with TOF-ERDA measurement from a film deposited under identical conditions. Both techniques show a close to stoichiometric film composition with respect to ZrN and AlN. The O concentration comes out lower for APT (0.19 at. %) than for TOF-ERDA (1.7 at. %), corresponding to a difference of 1.51 at. %, and this is the largest deviation between the two measurements. Furthermore, the APT measurements indicate five times more Ar than the TOF-ERDA measurement. The Ar ions show a strong tendency for clustering, while the O ions exhibits an even distribution in general, except for a small volume with high amounts of oxides and water residues found in one of the tips.

Nanolabyrinthine structure
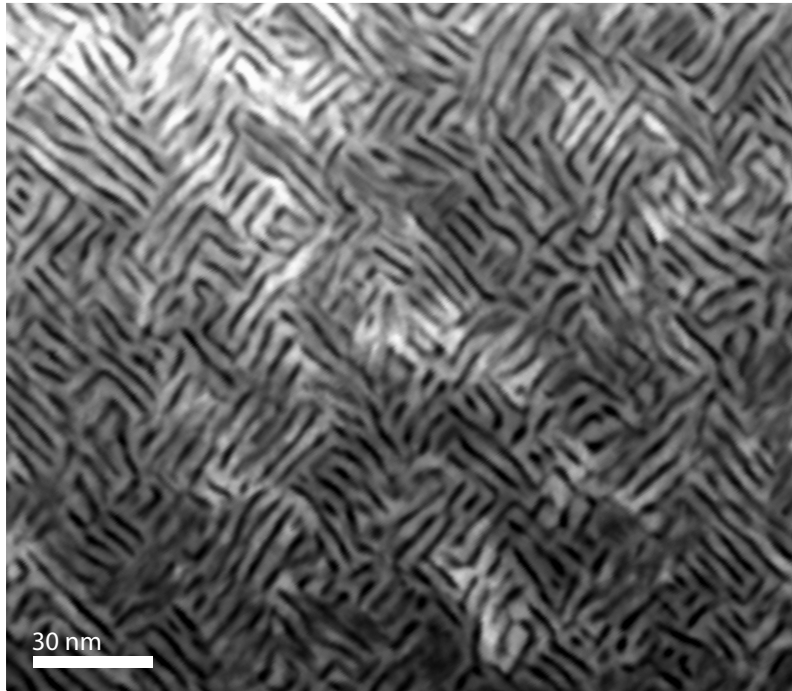
Figure 2: Plan view STEM micrograph of the self-organized labyrinthine structure in the sputtered

$Zr_{0.64}Al_{0.36}N$ thin film.
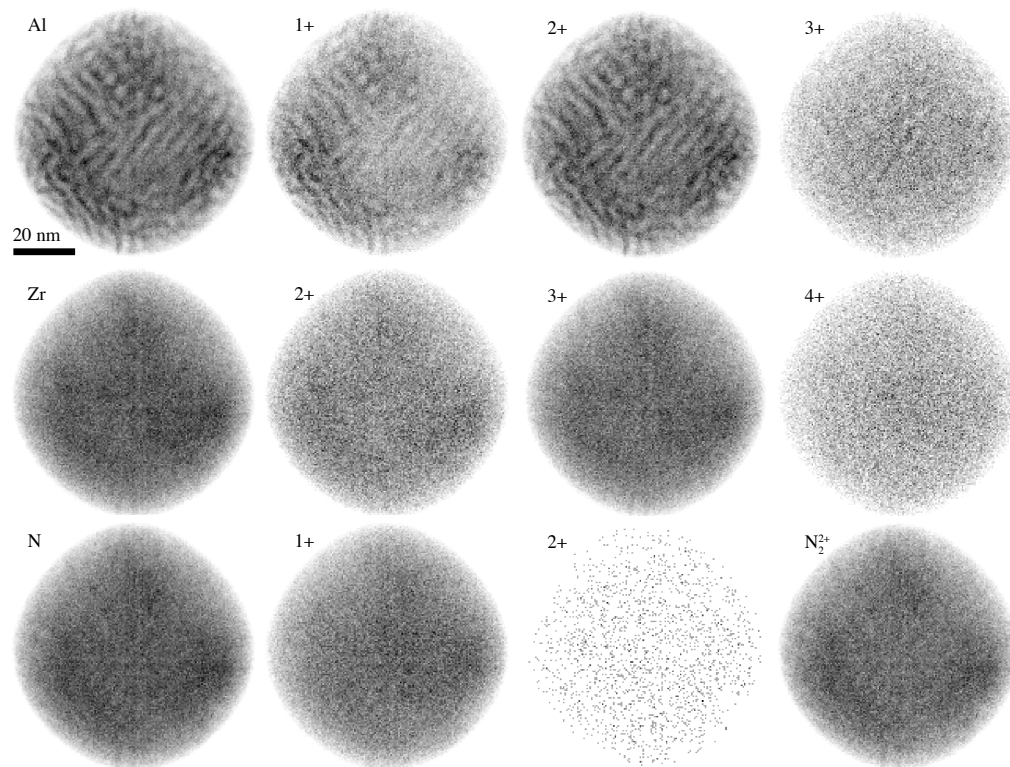
Figure 3: Projected ion maps for Zr, Al, and N, summed and for their respective ions.

The nanostructure of the films consists of AlN-rich platelets with a hexagonal (h) crystal structure sandwiched between ZrN-rich platelets with a face center cubic (fcc) crystal structure, as shown in Fig. 2 imaged by HAADF-STEM in plan-view and reported in [13]. The local crystallographic relationship is $(001)_{ZrN}//(0001)_{AlN}$ and $<110>_{ZrN}//<2\text{-}1\text{-}10>_{AlN}$. Fig. 3 shows that APT can resolve this nanostructure by reconstruction where the Al, Zr, and N ions are binned in squares (5 Å sides) disregarding the z-coordinates. The image contrast is given from zero ions (white) to the maximum number of ions per box (black) for each species. The Al image corresponds well with the TEM observations, with thin Al-rich plates between somewhat thicker Al-deficient ones, while the Zr and N images lack such features. This is dissimilar from TiAlN, where signs of spinodal decomposition can be seen in both Ti and Al ion maps [3]. In addition, the difference in N vacancies between AlN and TiN will make the N distribution inhomogeneous. Given the similarities of TiN and ZrN, combined with the density difference of AlN and ZrN, one would expect to find traces of the lamellae pattern in the Zr and N images as well. The loss of structural information in the Zr and N signals, taken together with the indications of two separate evaporation fields (see above), suggest that strong local magnification effects [21, 22] are present and affect the reconstructions. The TEM and APT length scales are in relatively close agreement when measured as the characteristic period (width) of the structure, ~3.8 nm from TEM and ~4.2 nm for the APT reconstruction, so the calibration of the mean evaporation field from the apex curvature was nearly correct. The stronger bonds in the fcc-ZrN-rich phase require a locally higher field than the h-AlN-rich phase to maintain equal evaporation rates, which will result in protrusions of ZrN against the mean curvature of the evaporating tip. This, in turn, locally magnifies the species evaporating from the fcc-domains, and they will appear

in part to originate from the hexagonal domains as the current reconstruction algorithms assume an ideal evaporation surface [23].

Looking at the various charge states of Al in detail, given in Fig. 3 for Al^{1-3+}, shows that the signal-to-noise ratio varies between the different states. Al^{2+} has the best signal quality, and Al^+ retains a significant amount, while the Al^{3+} image only contains a very weak signal and is dominated by noise. The various Zr and N (and N_2) charge states mainly show homogeneous noise along with features exhibiting four-fold symmetry, which is consistent with the crystallographic orientation of the sample ([001] lies along the tip axis, with [100] along the x-direction of the detector). The exception is N^{2+}, where the structure seen for the Al ions is faintly visible in the middle of the image. The lack of signal in the Al^{3+}, Zr^{2-3+}, and N^+ images, taken together with the Kingham analysis above, suggests that those ions mostly originated from high-field regions with a corresponding high local curvature, which would be responsible for the smearing of the ion trajectories. These regions would then correspond to the cubic ZrN phase, as those bonds are known to be stronger (cf. Kingham analysis above). The probable existence of Zr ions post-ionized in low fields would stem from ions evaporated from the low-field phase or from ions whose trajectories cross over into the low-field regions, hence it is not possible to categorically assign those ions to either the cubic or the hexagonal domains, although the lack of structural information suggests that the latter mechanism dominates.
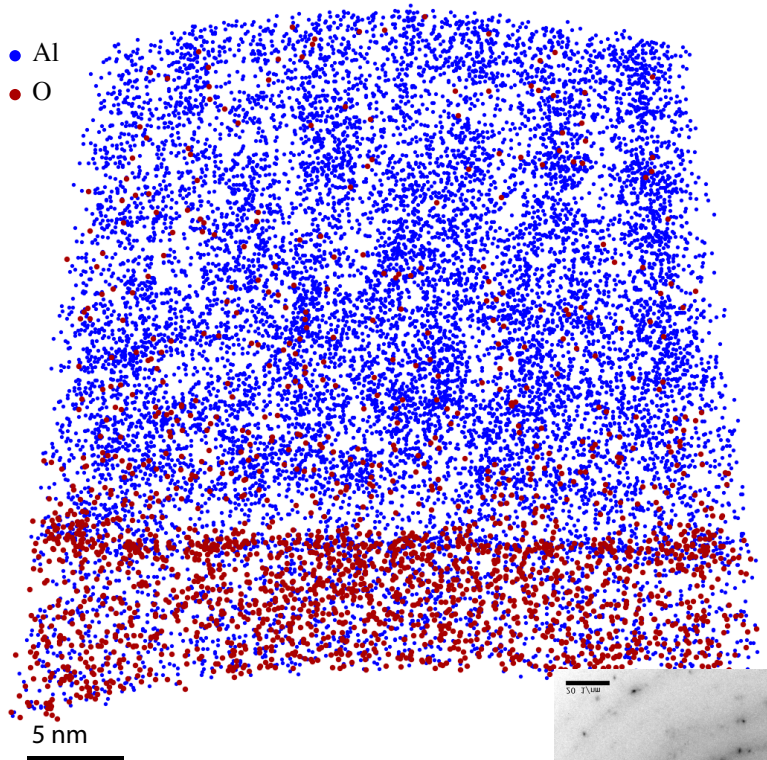
Figure 4: Cross sectional atom map of the film-subst[...]ce of self-organization. Al atoms are shown in blue and O[...]
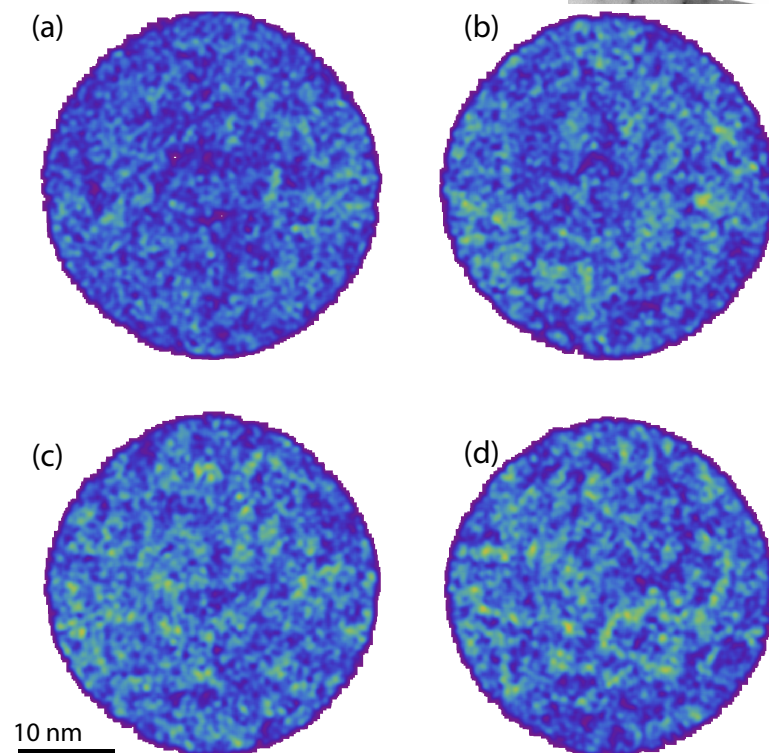
Figure 5: Al maps from (a) the substrate and up to (d) 8 nm from the interface, taken with 2 nm slice thicknesses and Gaussian broadening of the position of each Al atom.

Initial Growth

During one APT run of a tip from the 800 °C sample, the film-substrate interfacial region was serendipitously analyzed without any specimen failure, which is otherwise a common occurrence in APT when analyzing across interfaces of different phases. An Al atom map for a slice running through the tip is shown in Fig. 4. At the top the nanostructure of the steady state growth is visible, which originates about 5-8 nm above the substrate, beneath which there is a smooth transition from a disordered yet segregated structure. Just above the MgO substrate a thin region of apparently low density is visible, which is a reconstruction artifact from the changing field evaporation conditions of the ZrAlN and the MgO [24]. As noted above, there is very little structural information contained in the Zr and N atom maps, due to the local magnification of the ZrN domains, which are consequently not shown here.

The region closest to the substrate is interesting as it records the onset of self-organization and how it evolves over a few nanometers (or ~20 monolayers). This evolution is shown in more detail in Fig. 5, which presents the absolute distribution of Al atoms in 2 nm thick slices from (a) the substrate to (d) 8 nm above in 2 nm steps. To further reduce the noise, each ion is represented by a Gaussian distribution with a standard deviation of 7 Å. Fluctuations are present from the start, but appear random and without structure. As the growth continues the fluctuations grow in magnitude and in lateral extent. After 7-8 nm the separation has self-organized in the steady-state labyrinthine structure described above.

The increasing segregation with growth tallies with a surface-diffusion-driven segregation, that for each layer acts as a template promoting increased separation for the next. Initially, no site on the substrate is more preferable than the other for either

Zr or Al atoms, and random fluctuations will appear. During deposition of each successive atomic layer these variations will introduce a variation in the energy of surface atoms depending on the chemical identity and composition of the underlying layers. The segregation tendency is mitigated by entropic effects, and there are features that grow in Al content over 1-2 nm and then diminish again, so the process is not fully deterministic. The emergence of the ordered growth first appears abruptly at ~6 nm from the interface, but only locally, as seen by the change from diffuse segregated domains into segregated domains organized along the <110> directions.

During steady-state growth AlN forms the equilibrium hexagonal crystal structure in the present films [13], after having nucleated at some point on the otherwise cubic growth front. Before this nucleation there should not exist any strong crystallographic anisotropy driving the segregation, but the hexagonal phase has only mirror symmetry with regards to the cubic template and matrix, leading to strong (semi)coherency strain. It is therefore likely that the emergence of order along the <110> directions coincides with the nucleation of hexagonal domains, which in turn requires Al domains large enough to make the transformation energetically favorably.

Breakdown of nanolabyrinthine growth by ZrN precipitation

a

b

owing the

the

15 nm
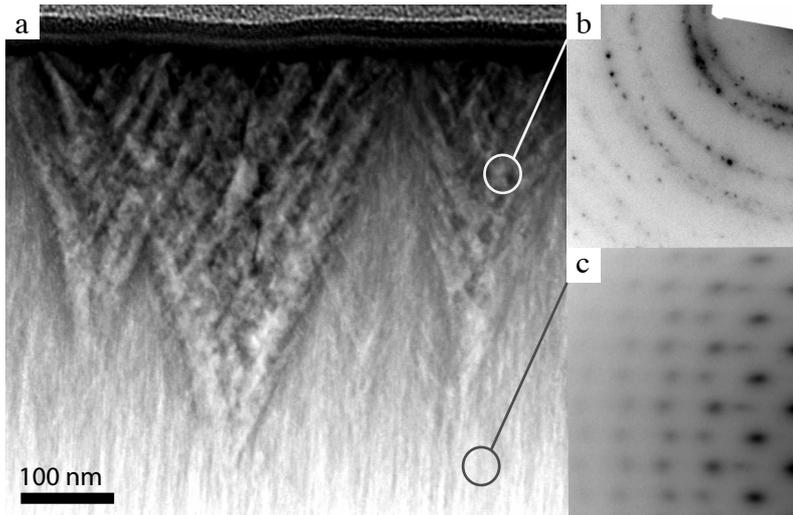
Figure 7: Atom probe of a ZrN precipitate in the $Zr_{0.64}Al_{0.36}N$ thin film grown at 900 °C. Zr atoms in green, Al atoms in blue.

In the sample deposited at 900 °C, the regular nanolabyrinthine growth was interrupted locally, as shown in the cross-sectional HAADF-STEM micrograph in Fig. 6 (a). The Z-contrast displays a disorganized region that grows in a wedge shape expanding up towards the film surface. The selected-area electron diffractogram (SAED) in Fig. 6 (b) from this region shows a polycrystalline equiaxed grain structure with a fcc diffraction pattern, which may be compared with that of the organized

structure in Fig. 6 (c), i.e., in the disorganized regions the crystallographic relationship between h-AlN and fcc-ZrN that is present in the organized nanolabyrinthine regions is lost. The disorganized regions are likely of limited lateral extent, as further thinning of the sample revealed the self-organized labyrinthine structure beneath one of the regions.

The wedge-shaped regions were also imaged in four APT runs; an atom map from one such analysis is shown in Fig. 7. Two distinct sub-domains are visible, relatively large ($\approx$50 nm in diameter) pure ZrN domains, and in between them a thinner region with random Al-Zr fluctuations. The thin Al-rich regions do not give rise to any diffraction lines in addition to the fcc-ZrN lines, which suggest that they are amorphous or highly distorted. Observations of crystallographically distorted AlN-rich nanobricks have been reported for arc evaporated ZrAlN, which in lattice resolved TEM imaging at least patchwise resembled the wurzite structure [25]. Based on these previous observations and the relatively high Al-content we propose these regions to be distorted wurtzite-AlN with dissolved Zr. The proxigram [26] of Fig. 7 is shown in Fig. 8, where the reference interface was taken in the middle of the transition from ZrN to the bulk composition. It shows that there is virtually no Al in the ZrN, but these regions show an accumulation of the carbon impurities to a level of 2-3 at. %. There is also a classical downhill diffusion profile present, as the Zr content has a minimum just at the interface, and then rises to the bulk value when moving farther from the ZrN precipitate. A jog in the N stoichiometry is observed at the interface (which is still present if N+C is considered). Similar features have been observed by APT in the Ti-Al-N system [3, 16] in the case of spinodal decomposition, but it is unclear whether it was due to variations in absolute N or metal concentrations, and the same situation occurs here.
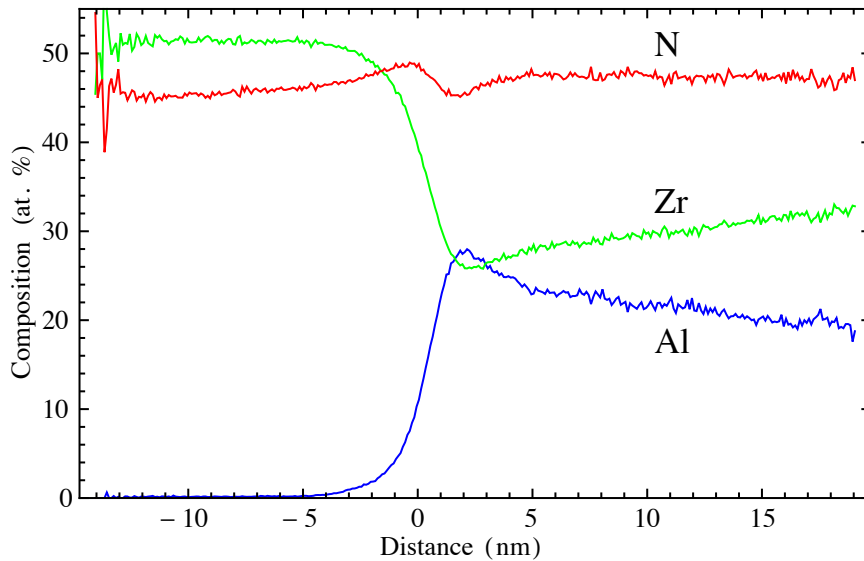
Figure 8: Proxigram taken at a boundary to a ZrN precipitate from the Sample in Fig 7, showing downhill diffusion of Zr, and defect accretion at the boundary in the N signal.

The wedge-shape regions thus consist of ZrN precipitates in an AlN-rich matrix. The shape of these regions points towards a competitive growth mode, where they outgrow the parent self-organized structure. The underlying phenomenon for (111)-oriented grains outgrowing (200) grains is inferred by comparing with TiN, where the diffusion of Ti on the (200) planes is higher than on (111), which leads in turn to their preferential growth [27]. The situation appears similar here, where the vicinity of the ZrN precipitates is perturbed from the steady-state growth. From the diffusion profile in Fig. 8 we see that the ZrN grains act as sinks for Zr, which provides the necessary drift tendency for a net diffusive flow into the precipitates. The ZrN precipitates continue to grow in this manner until their surfaces become too large for Al to diffuse out from them, causing a disorganized segregated structure to form again, probably together with renucleation as indicated by the SAED pattern in Fig. 6 (b).

Conclusions

Atom probe tomography has been used to analyze self-organized nanostructured Zr(Al)N/Al(Zr)N thin films composed of interleaved nm-thick lamellae, grown by

magnetron sputtering at 800 and 900 °C. The APT spectra were qualitatively similar to those reported for TiN-based alloys like TiAlN and TiSiN. The nanostructure was recovered in the Al signal, with the scale in good agreement with TEM observations, while trajectory aberrations caused information loss in the case of Zr (and likely N as well), hindering compositional measurements of the constituent phases. The initial evolution of the self-organization was imaged in one run that went through to the MgO substrate. A disordered segregation started in the first nm from the substrate, and increased in amplitude over ~8 nm until the system transformed locally into the steady-state growth mode of lamellae. When deposited at 900 °C the self-organization was unstable against precipitation of pure ZrN grains.

Acknowledgements

References

[1]   T. Kelly, D. Larson, MRS Bulletin 37 (2012) 150.

[2]   A. Hörling, L. Hultman, M. Odén, J. Sjölén, L. Karlsson, Journal of Vacuum Science and Technology A 20/5 (2002) 1815.

[3]   L.J.S. Johnson, M. Thuvander, K. Stiller, M. Odén, L. Hultman, Thin Solid Films 520/13 (2012) 4362.

[4]   A. Knutsson, J. Ullbrand, L. Rogström, N. Norrby, L.J.S. Johnson, L. Hultman, J. Almer, M.P.J. Jöesaar, B. Jansson, M. Odén, Journal of Applied Physics 113/21 (2013) 213518.

[5]   Veprek, S., Reiprich, S., Shizhi, Li, Applied Physics Letters 66/20 (1995) 2640.

[6]   F. Vaz, L. Rebouta, P. Goudeau, H. Garem, J.P. Rivière, A. Cavaleiro, Surface & Coatings Technology 133-134 (2000) 307.

[7] A. Flink, M. Beckers, J. Sjölén, T. Larsson, S. Braun, L. Karlsson, L. Hultman, Journal of Materials Research 24/8 (2009) 2483.

[8] L. Rogström, M.P. Johansson, N. Ghafoor, L. Hultman, M. Odén, Journal of Vacuum Science and Technology A 30/3 (2012) 031504.

[9] B.M. Howe, E. Sammann, J.G. Wen, T. Spila, J.E. Greene, L. Hultman, I. Petrov, Acta Materialia 59/2 (2011) 421.

[10] D. Holec, R. Rachbauer, L. Chen, L. Wang, D. Luef, P.H. Mayrhofer, Surface and Coating Technology 206/7 (2011) 1698.

[11] R. Lamni, R. Sanjines, M. Parlinska-Wojtan, A. Karimi, F. Levy, Journal of Vacuum Science and Technology A 23/4 (2005) 593.

[12] S. PalDey, S.C. Deevi, Material Science and Engineering A 342/1-2 (2003) 58.

[13] N. Ghafoor, L.J.S. Johnson, D.O. Klenov, J. Demeulemeester, P. Desjardins, I. Petrov, L. Hultman, M. Odén, APL Materials 1 (2013) 022105.

[14] K. Thompson, D. Lawrence, D.J. Larson, J.D. Olson, T.F. Kelly, B. Gorman, Ultramicroscopy 107/2-3 (2007) 131.

[15] F.Z. Tang, B. Gault, S.P. Ringer, J.M. Cairney, Ultramicroscopy 110/7 (2010) 836.

[16] R. Rachbauer, S. Massl, E. Stergar, P. Felfer, P.H. Mayrhofer, Surface & Coatings Technology 204/11 (2010) 1811.

[17] J. Martan, P. Benes, Thermochimica Acta 539 (2012) 51.

[18] D.R. Kingham, Surface Science 116/2 (1982) 273.

[19] F. Tasnádi, I.A. Abrikosov, L. Rogström, J. Almer, M.P. Johansson, M. Odén, Applied Physics Letters 97/23 (2010) 231902.

[20] A. Knutsson, I.C. Schramm, K.A. Grönhagen, F. Mücklich, M. Odén, Journal of Applied Physics 113/11 (2013) 114305.

[21] F. Vurpillot, A. Bostel, D. Blavette, Applied Physics Letters 76/21 (2000) 3127.

[22] M.K. Miller, M.G. Hetherington, Surface Science 246/1-3 (1991) 442.

[23] B. Gault, D. Haley, F. de Geuser, M.P. Moody, B.A. Marquis, D.J. Larson, B.P. Geiser, Ultramicroscopy 111/6 (2011) 448.

[24] D.J. Larson, T.J. Prosa, B.P. Geiser, W.F. Egelhoff, Ultramicroscopy 111/6 (2011) 506.

[25] L. Rogström, L.J.S. Johnson, M.P. Johansson, M. Ahlgren, L. Hultman, M. Odén, Scripta Materialia 62/10 (2010) 739.

[26] O.C. Hellman, J.A. Vandenbroucke, J. Rusing, D. Isheim, D.N. Seidman, Microscopy and Microanalysis 6/5 (2000) 437.

[27] D. Gall, S. Kodambaka, M.A. Wall, I. Petrov, J.E. Greene, Journal of Applied Physics 93/11 (2003) 9086.